EPR imaging: The relationship between CW spectra acquired from an extended sample subjected to fixed stepped gradients and the Radon transform of the resonance density

Benjamin B. Williams [a,c,1], Xiaochuan Pan [b,c], Howard J. Halpern [a,c,*]

[a] Department of Radiation and Cellular Oncology, University of Chicago, Chicago, IL, USA
[b] Department of Radiology, University of Chicago, Chicago, IL, USA
[c] Center for EPR Imaging in Vivo Physiology, University of Chicago, Chicago, IL, USA

Abstract

EPR spectroscopy can be extended to a spectroscopic imaging modality by applying magnetic field gradients across the sample to encode spatial information in the measured spectra. In this work, we present a mathematical model of the EPR imaging process in terms of the Radon transform. We describe a model for electron paramagnetic resonance imaging, derive its explicit relationship to the Radon transform, and discuss several options for reconstructing the sample absorption and dispersion densities. An important extension to previous descriptions is the incorporation of large amplitude magnetic field modulation, which can be used to improve the signal-to-noise ratio for continuous wave signal acquisition. Magnetic field modulation is shown to cause well understood changes in the shapes of spectra in the reconstructed images, but does not affect the spatial resolution achieved in these images. Since many of the novel image reconstruction strategies and noise filtering algorithms that have been developed for other modalities start from this formalism, this work allows for their direct application to EPR imaging. This promises to lead to further improvements in EPR imaging techniques.
© 2005 Elsevier Inc. All rights reserved.

Keywords: EPR; EPRI; Tomography; Overmodulation; Radon transform

1. Introduction

1.1. Capabilities, challenges, and motivation for the theoretical model

Electron paramagnetic resonance imaging (EPRI) is a technique capable of measuring the spatial and spectral distribution of the absorption and dispersion of RF energy by an extended sample of paramagnetic probes [1,2]. Images of water soluble probes that have been injected into animals provide high sensitivity physiologic information [3–7]. These radicals, or spin probes, are designed to be sensitive to specific aspects of physiology [8]. Using a variety of spin probes, measurable quantities include, but are not limited to, the distribution of endogenous or introduced paramagnetic species [9–11], tissue redox status [12], pH [13], and microviscosity [14]. One particular measurement that has received significant attention is the measurement of tissue oxygen concentration [5,10,15].

Recent advances in spin probe chemistry and spectrometer design have addressed some of the challenges inherent in EPRI, thereby increasing sensitivity and

---

* Corresponding author. Fax: +1 773 702 5940.
  E-mail address: h-halpern@uchicago.edu (H.J. Halpern).
[1] Present address: Department of Radiology, Dartmouth Medical School, Hanover, NH 03755, USA.

List of symbols

Functions

$f(B, \vec{x})$	Spectral–spatial object, 4D EPR density, has both absorption and dispersion components
$f_{sw}(B, \vec{x})$	Spectral–spatial object, centered about B_0
$f_{\vec{r}}(\vec{r})$	Spectral–spatial object, expressed as a function of $(B, c\vec{x})$, centered about B_0
$\tilde{f}_{\vec{r}}(\vec{r}; B_m)$	First harmonic representation of the spatial spectral object, $f_{\vec{r}}(\vec{r})$, for a given modulation amplitude and frequency
$p(\xi, \hat{\alpha}_{\vec{G}})$	Radon transform of $f_{\vec{r}}(\vec{r})$
$s_\xi(\xi, \vec{G})$	Measured EPR spectra, in terms of normalized distance along projection axis
$s(B_{sw}, \vec{G})$	Measured EPR spectra
$\tilde{s}_\xi(\xi, \vec{G})$	First harmonic EPR signal for a given modulation amplitude and negligible modulation frequency

Roman characters

B_{TOT}	Magnetic field strength, from applied and microscopic sources, orthogonal to the excitation field
$\vec{B}_1$	Magnetic field component of the RF excitation wave
B	Strength of the applied magnetic field
B_{v_0}	Magnetic field corresponding to v_0 for EPR
ΔB	Magnetic field range of the EPR signal without an applied magnetic field gradient
$B_{app}(\vec{x})$	Applied magnetic field
B_{sw}	Applied, spatially uniform magnetic field offset from B_0 used to sweep the field across the resonance
B_0	Applied static magnetic field
ΔB_{sw}	Sweep width, range over which the magnetic field must be swept to cover the resonance
$\Delta B_{sw,alt}$	Sweep width, defined to produce projections of uniform length
$B_{mod}(t)$	Modulated magnetic field strength
B_m	Amplitude of the modulated magnetic field
$B'(t)$	Temporary magnetic field used for calculating the effect of modulation on images

c	Scalar constant relating magnetic field units and spatial units
$\vec{G}$	Applied magnetic field gradient
G	Applied magnetic field gradient magnitude, positive definite
$\hat{G}$	Applied magnetic field gradient direction
G_{max}	maximum gradient magnitude
g	g-factor
h	Planck's constant
ΔL	Diameter of spherical spatial support of the spatial–spectral object
$O(B_m^2, t)$	Taylor series terms proportional to 2nd or higher orders of B_m
$\vec{r}$	Cartesian coordinates in the image space
$r'(t)$	Temporary image coordinates used for calculating the effect of modulation on images
t	Time
$\mathcal{R}^{-1}$	Inverse Radon transform operator
T	Period of the modulated magnetic field
$\vec{x}$	3D spatial position
$x'(t)$	Temporary spatial position used for calculating the effect of modulation on images

Greek characters

$\hat{\alpha}_{\vec{G}}$	Unit vector describing the applied magnetic field direction
α	Angle normal to lines of integration with respect to the B-axis in a $\{B, \kappa\}$ space
β	Bohr magneton
$\Delta_{B_{sw}}$	Magnetic field sampling interval
Δ_ξ	Projection sampling interval
κ	Spatial axis defined by the cross-product of $\vec{G}$ and $\vec{x}$
v	RF excitation frequency
v_0	Experimental RF excitation frequency
ξ	Normalized distance along the projection axis
$\xi'(t)$	Projection of the modulated magnetic field with opposite sign
ω_m	Frequency of the modulated magnetic field
$\Omega_{\vec{r}}$	Spatial support of the spectral–spatial object, in terms of $\vec{r}$
$\Omega_{\vec{x}}$	Spatial support of the spectral–spatial object, in terms of $\vec{x}$

extending in vivo applicability to larger subjects. Water soluble spin probes with overall peak-to-peak linewidths as low as 2.5 μT and transverse relaxation times of as large as 12 μs (spin packet linewidth of ~0.5 μT) at both X-band and 250 MHz have been developed [16,17]. This increases the signal-to-noise ratio (SNR) of the EPRI measurements and the sensitivity to oxygen. The development of EPR spectrometers using low excitation frequencies has enabled successful EPRI of in vivo physiology using small rodents [18–22]. In vivo EPR imaging is being performed at frequencies near the 200 MHz excitation frequency commonly used in 4.7 T MRI systems and significantly lower than the frequencies used for recent high field MRI [23]. Resonator sys-

tems have been designed for large, lossy, and living samples [24–26]. Coupled with the unique ability of EPR imaging for certain physiologic measurements, these advances have led to increased interest in EPR imaging over the past several years.

1.2. Previous research: Acquisition of EPRI data

It was recognized independently in NMR [27] and in EPR [28,29] that magnetic resonance spectra acquired with static linear magnetic field gradients established across sample may be interpreted as projections of an object with an intrinsic spectral dimension. Due to the rapid relaxation of the EPR resonance, ranging from ns to several microseconds, EPR image data are collected with fixed stepped gradients and either pulsed or continuous wave (CW) spin excitation. These initial papers describe the theory for acquiring and reconstructing 2D spectroscopic images. Results include the relationship between the gradient magnitude and the spectral projection angle and the range conversion and scaling factor that relate the acquired spectral data to the desired image projections. Spectroscopic images can then be reconstructed using conventional image reconstruction techniques [30].

The current work augments these and subsequent papers that demonstrate 3D [31] and 4D [32] spectroscopic EPR imaging by providing a precise mathematical description of the relationship between the acquired spectra and the Radon transform and by defining the effects of Zeeman modulation [33]. Such a description is necessary to optimize the sensitivity of the technique and the accuracy of the physiologic information derived from EPR images. A precise theoretical model of EPR imaging will enable the development of novel algorithms of image acquisition, processing, and reconstruction and provide a general basis for iterative approaches to image reconstruction. In this work, we describe a model for spectroscopic EPRI, derive its relationship to the Radon transform, and discuss several options for reconstructing the resonance distribution and estimating the spectral parameters of interest.

1.3. Data collection with large modulation amplitude

CW-EPR spectra measured using overmodulation, defined as Zeeman modulation amplitudes greater than one-tenth to one-third the overall peak-to-peak linewidth, become increasingly distorted as the amplitude of the modulation rises [34]. Accompanying this distortion is a sharp increase in the signal amplitude as the modulation amplitude approaches the width of the spectral features and then a gradual decrease after this point. Accordingly, overmodulation can be used to increase the SNR of measured spectra. However, without an accurate model to account for the spectral distortion it

is difficult to obtain accurate estimates of the underlying spectral parameters, such as the intrinsic Lorentzian linewidth. In order to overcome this limitation, several algorithms have been presented that model the effect of modulation amplitude on measured spectra and allow estimation unbroadened linewidths [35,36]. Recently a model which accurately accounts for the effects of both modulation amplitude and frequency on the recorded spectra has been described with an accompanying efficient spectral fitting algorithm [37]. Using this model, spectral parameters can be accurately and precisely estimated over the range of practical modulation amplitudes and frequencies, while allowing operation at a much higher SNR [38].

A key question that needs to be addressed using high modulation for EPR image acquisition is the effect of modulation on the spatial resolution of the spectral–spatial image. Naively, one may expect that an increased modulation amplitude would blur reconstructed spectroscopic images and decrease their spatial resolution. A principle result of this paper is that the effects of overmodulation are propagated solely into the spectral distributions in the reconstructed image, in a clearly defined manner; spatial resolution is unaffected by the large modulation amplitudes.

2. Theory

2.1. EPR with an applied magnetic field gradient

The absorption of energy at RF by an unpaired electron prepared in a magnetic field occurs when the photon energy equals the electron Zeeman energy splitting. This resonance condition can be expressed as

$$hv = g\beta B_{\text{TOT}}, \tag{1}$$

where h is Planck's constant, v is the frequency of the RF wave, g is the g-factor, β is the Bohr magneton, and B_{TOT} is the strength of the main magnetic field which is taken to be orthogonal to the RF magnetic field $\vec{B}_1$. The magnetic field, B_{TOT}, is a sum of applied magnetic fields and microscopic fields generated by inter- and intramolecular paramagnets.

For irradiation with a fixed frequency v_0 an ensemble of electrons will have a four-dimensional spectral–spatial resonance density $f(B, \vec{x})$. This density describes the sum of the absorption and dispersion per unit volume and per unit magnetic field at spatial location $\vec{x}$ for an externally applied magnetic field with strength B. This intensity distribution will be referred to as the *spectral–spatial object*. The data obtained in the imaging process give an estimate of the spectral–spatial object which we will call the *spectral–spatial image*. We assume that $f(B, \vec{x})$ is a bounded function with finite support over the range $[B_{v_0} - \frac{\Delta B}{2}, B_{v_0} + \frac{\Delta B}{2}] \times \Omega_{\vec{x}}$, where

$B_{v_0} \equiv h v_0 / g\beta$, ΔB is the magnetic field interval that must be fully sampled, and $\Omega_{\vec{x}}$ is the spatial support with diameter ΔL. The spectral distribution is not strictly bounded, as it is composed of Lorentzian components; however, intensity in the tails of the spectrum become negligibly small and an effective bound may be used. Typically, absorption spectra are measured over the larger of the ranges of roughly 10–40 times the HWHM of the intrinsic Lorentzian components and seven times the peak-to-peak linewidth.

The applied magnetic field $B_{\text{app}}(\vec{x})$ consists of the spatially invariant static and swept main magnetic fields B_0 and B_{sw} and the spatially varying magnetic gradient field $\vec{G} \cdot \vec{x}$,

$$B_{\text{app}}(\vec{x}) = B_0 + B_{\text{sw}} + \vec{G} \cdot \vec{x}. \tag{2}$$

This assumption of gradient linearity is necessary to describe this situation using the standard Radon transform. However, gradient non-uniformities can be naturally described using the generalized Radon transform [39–41]. Here, B_0 is a static field whose magnitude is set near that of the resonance field, B_{v_0}, and B_{sw} is a variable offset from B_0 used to sweep the field over the range of the resonance. The magnitude and direction of the magnetic field gradient are given by $G = |\vec{G}|$ and $\hat{G} = \vec{G}/G$, respectively. Here, $G \in [-G_{\text{max}}, G_{\text{max}}]$, where G_{max} is a maximum gradient magnitude and $\hat{G}$ varies over 2π steradians, or one hemisphere in the spatial domain. Note that spatially varying error terms due to inhomogeneities in the nominally spatially invariant components B_0 and B_{sw} and nonlinearities in the spatially varying term may be naturally included in Eq. (2).

In a 4D $\{B, \vec{x}\}$ space, the resonance condition $h v_0 = g\beta B_{\text{app}}(\vec{x})$ defines a hyperplane over which electrons will be excited. For a given $B_{\text{app}}(\vec{x})$, an integral over this hyperplane,

$$\int_{B_0 - \frac{\Delta B}{2}}^{B_0 + \frac{\Delta B}{2}} \int_{\Omega_{\vec{x}}} f(B, \vec{x}) \delta(B - B_{\text{app}}(\vec{x})) \, \mathrm{d}\vec{x} \, \mathrm{d}B, \tag{3}$$

will contribute to the signal measured at a particular B_{sw}. This represents the projection of the signal from the hyperplane onto an orthogonal line traversed by varying B_{sw}. The spectrum, $s(B_{\text{sw}}, \vec{G})$, is given by integration over the set of hyperplanes defined by Eq. (3) as B_{sw} is varied. Using Eq. (2) in Eq. (3) yields

$$s(B_{\text{sw}}, \vec{G}) = \int_{B_0 - \frac{\Delta B}{2}}^{B_0 + \frac{\Delta B}{2}} \int_{\Omega_{\vec{x}}} f(B, \vec{x}) \delta(B - (B_0 + B_{\text{sw}} + \vec{G} \cdot \vec{x})) \, \mathrm{d}\vec{x} \, \mathrm{d}B, \tag{4}$$

which may be re-expressed in terms of $f_{\text{sw}}(B, \vec{x}) \equiv f(B_0 + B, \vec{x})$ as

$$s(B_{\text{sw}}, \vec{G}) = \int_{-\frac{\Delta B}{2}}^{+\frac{\Delta B}{2}} \int_{\Omega_{\vec{x}}} f_{\text{sw}}(B, \vec{x}) \delta(B - B_{\text{sw}} - \vec{G} \cdot \vec{x}) \, \mathrm{d}\vec{x} \, \mathrm{d}B. \tag{5}$$

Such EPR spectra, collected with and without a magnetic field gradient, and their interpretations as projections of a spectral–spatial object is demonstrated in Fig. 1. For a spatially uniform magnetic field, the recorded spectrum can be regarded as a projection of the spectral–spatial object onto the spectral axis. Here, integration occurs over all spatial coordinates. This is shown in Fig. 1A for a two-dimensional object consisting of three samples with spectra with the same centers
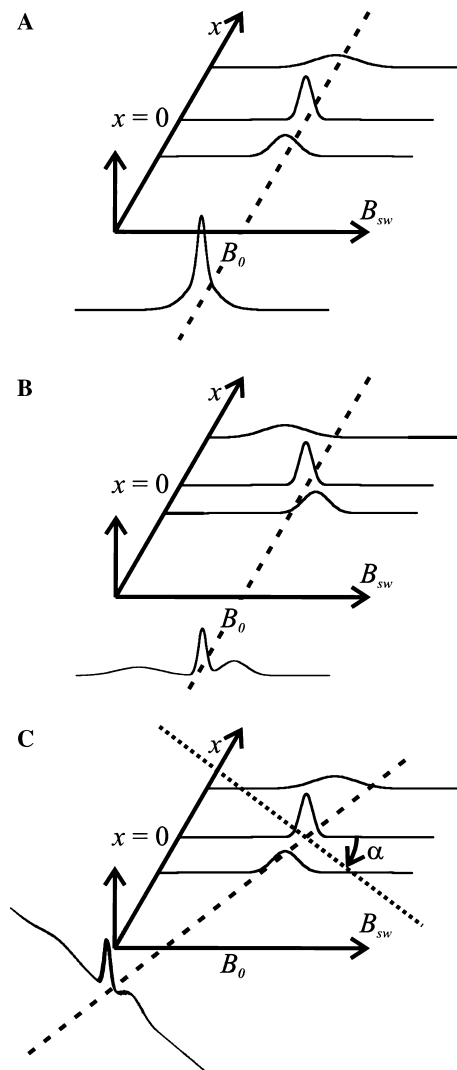

Fig. 1. Shown is the effect of a linear magnetic field gradient on spectra recorded for a two-dimensional spectral–spatial object and the interpretation of these spectra as the Radon transform of the object. Lines of integration are denoted by dashed lines and in (C) the dotted line is parallel to the projection axis. (A) Without an applied magnetic field gradient, the recorded spectrum is the sum of the individual spatial components or a projection of the object onto the spectral axis. (B) When a small positive gradient is applied, the individual spatial components pass through resonance at values of B_{sw} that depend on the their spatial positions and the components are resolved in the recorded spectrum. (C) With proper scaling, the spectrum shown in (B) can be interpreted as a projection of the spectral–spatial object with projection angle α.

but different widths. Imposing a linear magnetic field gradient along the x-axis effectively shears the object, with respect to B_{sw}, as shown in Fig. 1B. With this gradient, and integration of signal along lines perpendicular to the spectral axis, the individual spatial components are distinguishable in the recorded spectrum. Fig. 1C recasts the shearing process as a rotation of the lines of integration in the spectral–spatial space. This pictorially demonstrates that the acquisition of the RF absorption as a function of gradient direction, gradient amplitude, and sweeping magnetic field magnitude can be directly related to a Radon transformation of the spectral and spatial information from the sample. This establishes the general relationship between swept field EPR acquisition in the presence of fixed stepped gradients and the Radon transform. The following section establishes the formal relationship between the two.

2.2. Relation to the Radon transform without Zeeman modulation

For a given value of B_{sw}, the integration in Eq. (4) is carried out over the hyperplane specified by

$$B = B_{sw} + \vec{G} \cdot \vec{x} \tag{6}$$

in the four-dimensional space $\{B, \vec{x}\}$. This four-dimensional operation can be reduced to two dimensions by introducing a new variable

$$\kappa = c\hat{G} \cdot \vec{x}, \tag{7}$$

where c is a scalar constant with units of magnetic field strength over length. Note that κ has units of magnetic field strength. Setting $c = \Delta B/\Delta L$ is a useful option that facilitates uniform angular sampling in the spectral–spatial space. Using this variable, one can define an effective two-dimensional space, $\{B, \kappa\}$, with common units for both axes. Here, the hyperplane defined in Eq. (6) is collapsed to a straight line with a slope of $c^{-1}G$,

$$B = B_{sw} + G(\hat{G} \cdot \vec{x}) = B_{sw} + c^{-1}G\kappa. \tag{8}$$

The angle α, describing the angle between the normal to this line and the B-axis, is given by

$$\tan \alpha = -c^{-1}G, \tag{9}$$

where $\alpha \in [-\frac{\pi}{2}, \frac{\pi}{2}]$. Using Eq. (9), one can re-express Eq. (4) as

$$s(B_{sw}, \vec{G}) = \cos \alpha \int_{-\frac{\Delta B}{2}}^{+\frac{\Delta B}{2}} \int_{\Omega_{\vec{x}}} f_{sw}(B, \vec{x}) \delta(\cos \alpha B$$
$$- \cos \alpha B_{sw} + \sin \alpha c \hat{G} \cdot \vec{x}) \, d\vec{x} \, dB. \tag{10}$$

Finally, Eq. (10) can be written as

$$s(B_{sw}, \vec{G}) = \cos \alpha \int_{\Omega_{\vec{r}}} f_{\vec{r}}(\vec{r}) \delta(\xi - \hat{\alpha}_G \cdot \vec{r}) \, d\vec{r}, \tag{11}$$

where $f_{\vec{r}}(\vec{r}) = f_{sw}(B, \vec{x})$ and

$$\xi \equiv \cos \alpha B_{sw},$$
$$\vec{r} \equiv (B, c\vec{x}),$$
$$\hat{\alpha}_G \equiv (\cos \alpha, \sin \alpha \hat{G}), \tag{12}$$
$$\Omega_{\vec{r}} \equiv \left[\frac{\Delta B}{2}, \frac{\Delta B}{2}\right] \times c\Omega_{\vec{x}}.$$

The integral on the right-hand side of Eq. (11) is the 4D Radon transform of $f_{\vec{r}}(\vec{r})$, which is denoted by $p(\xi, \hat{\alpha}_G)$,

$$p(\xi, \hat{\alpha}_G) = \int_{\Omega_{\vec{r}}} f_{\vec{r}}(\vec{r}) \delta(\xi - \hat{\alpha}_G \cdot \vec{r}) \, d\vec{r}. \tag{13}$$

Therefore

$$s(B_{sw}, \vec{G}) = \cos \alpha p(\xi, \hat{\alpha}_G). \tag{14}$$

In practice, spectra for EPRI are collected as a function of ξ rather than B_{sw}; data points within each projection are separated by the same distance along the projection axis, rather than the same distance in absolute field units. With this convention, Eq. (14) may re-expressed as

$$s_\xi(\xi, \vec{G}) = \cos \alpha p(\xi, \hat{\alpha}_G), \tag{15}$$

where $s_\xi(B_{sw} \cos \alpha, \vec{G}) \equiv s(B_{sw}, \vec{G})$. To maintain a uniform sampling density in these projections, the sampling interval, in terms of magnetic field, must increase as the gradient magnitude rises. Defining Δ_ξ to be the projection sampling interval and $\Delta_{B_{sw}}$ to be the field sampling interval, we obtain

$$\Delta_{B_{sw}} = \frac{\Delta_\xi}{|\cos \alpha|}. \tag{16}$$

Given an estimate of $p(\xi, \hat{\alpha}_G)$, the spectral–spatial image can be reconstructed according to

$$f_{\vec{r}}(\vec{r}) = \mathcal{R}^{-1}[p(\xi, \hat{\alpha}_{\vec{G}})], \tag{17}$$

where $\mathcal{R}^{-1}$ is the inverse Radon transform.

2.3. Gradient magnitude and direction domain for acquisition of spectral–spatial images

For many applications of the 4D Radon transform, the sampled volume is a four-dimensional hyper-sphere. However, as we have discussed and expressed in Eq. (12), the spectral range in the 4D spectral–spatial objects considered here is independent of the spatial position. At each spatial position we wish to sample the spectral axis from $[\frac{\Delta B}{2}, \frac{\Delta B}{2}]$. Thus, the sampled volume is a hyper-cylinder, which encompasses a complete sphere in the spatial domain and the finite range $[\frac{\Delta B}{2}, \frac{\Delta B}{2}]$ in the spectral domain. This range of spectral and spatial coordinates has been chosen to ensure that sufficient data is obtained to provide an image of all spectral information within the interval $[\frac{\Delta B}{2}, \frac{\Delta B}{2}]$ and a spatial interval of $[\frac{\Delta L}{2}, \frac{\Delta L}{2}]$ along each of the three spatial axes. One approach to efficiently accomplishing this involves using

a changing range of B_{sw}. This range can be derived from the limits of integration and δ-function arguments seen in Eq. (10). According to these quantities, and assuming that $c = \Delta B / \Delta L$,

$$B_{sw} \in \left[-\frac{\Delta B}{2} - c \tan \alpha \frac{\Delta L}{2}, \frac{\Delta B}{2} + c \tan \alpha \frac{\Delta L}{2} \right]$$
$$= \left[-\frac{\Delta B}{2} (1 + \tan \alpha), \frac{\Delta B}{2} (1 + \tan \alpha) \right]. \quad (18)$$

The width of this range, often referred to as the sweep width, is given by

$$\Delta B_{sw} \equiv \Delta B [1 + \tan \alpha]. \quad (19)$$

Eq. (19) defines the minimum sweep width necessary to measure the entire signal within a rectangular field of view for a given gradient magnitude. Note that the sweep width varies with the gradient magnitude and leads to projections of varying length. An alternate definition of the sweep width that results in projections of uniform length has been presented [29]. According to this definition, again assuming that $c = \Delta B / \Delta L$,

$$\Delta B_{sw,alt} = \frac{\sqrt{2} \Delta B}{\cos \alpha}. \quad (20)$$

Using this definition, the sampled volume is the hypersphere that circumscribes the previously defined hypercylinder. This volume includes spatial regions known to be devoid of signal. Because of this, it is a less efficient definition of the sweep width than that of Eq. (19), but one that is useful in those practical situations where the image reconstruction routine does not accept projections with varying length.

2.4. Relation to the Radon transform with Zeeman modulation

To increase the SNR of measured spectra, the signal is modulated at an audio frequency, and narrow-band phase sensitive detection is used. This modulation is established by superimposing a sinusoidally time-varying, spatially uniform magnetic field onto the applied magnetic field. For modulation of amplitude $B_m > 0$ and angular frequency ω_m, the modulation field can be expressed as $B_{mod}(t) = B_m \sin \omega_m t$. Therefore the time varying resonance signal is given by

$$s_\xi(\xi + B_{mod}(t) \cos \alpha, \vec{G}). \quad (21)$$

The amplitude of the component of this signal that varies at the modulation frequency ω_m and in phase with a modulation reference signal is measured as a function of ξ. This signal, referred to as the first harmonic signal, can be expressed mathematically as

$$\tilde{s}_\xi(\xi, \vec{G}; B_m) = \frac{1}{T} \int_{-T}^{T} s_\xi(\xi + B_{mod}(t) \cos \alpha, \vec{G}) \sin \omega_m t \, dt, \quad (22)$$

where $T = 2\pi / \omega_m$ is the period of the modulation field and the modulation frequency is small relative to the spectral linewidth expressed in Hertz [42]. Note that Eq. (22) makes no assumption about a limit on the modulation amplitude. Specifically, it may be much larger then the linewidth, though the effects of this overmodulation must be addressed during image analysis as discussed in the following section on image reconstruction. For modulation amplitude sufficiently large to exceed the linear response limit, where, for example, passage effects occur, the description presented below breaks down.

Combining [15] and [22] one obtains,

$$\tilde{s}_\xi(\xi, \vec{G}; B_m) = \cos \alpha \frac{1}{T} \int_{-T}^{T} p(\xi - \xi'(t), \hat{\alpha}_G) \sin \omega_m t \, dt, \quad (23)$$

where

$$\xi'(t) = -\cos \alpha B_{mod}(t). \quad (24)$$

According to the shift-theorem for the Radon transform, the inverse Radon transform of $p(\xi - \xi'(t), \hat{\alpha}_G)$ yields a shifted distribution function $f_{\vec{r}}(\vec{r} - \vec{r}'(t))$, where $\vec{r}'(t) = (B'(t), c\vec{x}'(t))$ satisfies

$$\vec{r}'(t) \cdot \hat{\alpha}_G = \xi'(t). \quad (25)$$

This can be expanded into

$$\cos \alpha B'(t) + c \sin \alpha \hat{G} \vec{x}'(t) = -\cos \alpha B_{mod}(t). \quad (26)$$

By multiplying both sides of Eq. (26) by $\cos \alpha$ and carrying out the integration of α over 2π, one can show that

$$B'(t) = -B_{mod}(t). \quad (27)$$

Similarly, multiplying both sides of Eq. (26) by $\sin \alpha$ and carrying out the integration of α over 2π, one obtains

$$c\vec{x}'(t) = 0. \quad (28)$$

Therefore, the inverse Radon transform of Eq. (23) can be rewritten as

$$\mathcal{R}^{-1} \left[\frac{\tilde{s}_\xi(\xi, \vec{G}; B_m)}{\cos \alpha} \right] = \frac{1}{T} \int_{-T}^{T} f_{\vec{r}}(B + B_{mod}(t), c\vec{x})$$
$$\times \sin \omega_m t \, dt. \quad (29)$$

Note that differences between the right-hand side of Eq. (29) and $f_{\vec{r}}(\vec{r})$ appear only in the spectral dimension. Thus, the measured spatial distribution is unaffected by modulation and, assuming adequate sampling, the modulation amplitude does not affect the spatial resolution in reconstructed images, even for large modulation amplitudes.

2.5. Image reconstruction

Eq. (29) expresses the relationship between the measured first harmonic absorption spectra and the Radon

transform of the spectral–spatial object for modulation amplitudes within the linear response limit. It provides the foundation for reconstruction of the spectra–spatial image via one of the many inverse Radon transform algorithms [30]. For each of these algorithms, there are several alternative methods that may be used to reconstruct the image.

2.6. Approximate relationship accurate for small modulation amplitudes and frequencies

The first of these alternatives is applicable for modulation amplitudes much less than the widths of the spectral features in the absorption distribution and gives a direct estimate of $f_{\vec{r}}(\vec{r})$. $s_\xi(\xi, \vec{G})$ is differentiable with respect to ξ and can be expanded into a Taylor series:

$$s_\xi(\xi + B_{\mathrm{mod}}(t) \cos \alpha, \vec{G}) = s_\xi(\xi, \vec{G}) + \frac{\partial s_\xi(\xi, \vec{G})}{\partial \xi} \\ \times B_{\mathrm{mod}}(t) \cos \alpha + \mathrm{O}(B_{\mathrm{m}}^2, t), \tag{30}$$

where $\mathrm{O}(B_{\mathrm{m}}^2, t)$ denotes the terms in the series that are proportional to second or higher orders of B_m. Substituting Eq. (30) into Eq. (22) yields

$$\tilde{s}_\xi(\xi, \vec{G}; B_{\mathrm{m}}) = \frac{\partial s_\xi(\xi, \vec{G})}{\partial \xi} B_{\mathrm{m}} \cos \alpha \\ + \frac{1}{T} \int_T^T \mathrm{O}(B_{\mathrm{m}}^2, t) \sin \omega_{mt} \, \mathrm{d}t. \tag{31}$$

Because $\lim_{B_{\mathrm{m}} \to 0} \frac{\mathrm{O}(B_{\mathrm{m}}^2, t)}{B_{\mathrm{m}}} \to 0$, one obtains from Eq. (31) that

$$\lim_{B_{\mathrm{m}} \to 0} \frac{\tilde{s}_\xi(\xi, \vec{G}; B_{\mathrm{m}})}{B_{\mathrm{m}}} = \frac{\partial s_\xi(\xi, \vec{G})}{\partial \xi} \cos \alpha. \tag{32}$$

Using Eq. (14) in Eq. (32), one can thus establish a relationship between the Radon transform of the density function $f_{\vec{r}}(\vec{r})$ and the measured signal as

$$\frac{\partial p(\xi, \hat{\alpha}_G)}{\partial \xi} = \frac{1}{\cos^2 \alpha} \lim_{B_{\mathrm{m}} \to 0} \frac{\tilde{s}_\xi(\xi, \vec{G}; B_{\mathrm{m}})}{B_{\mathrm{m}}}. \tag{33}$$

For small modulation amplitudes, the measured signal gives an approximation of the limit in Eq. (33)

$$\lim_{B_{\mathrm{m}} \to 0} \frac{\tilde{s}_\xi(\xi, \vec{G}; B_{\mathrm{m}})}{B_{\mathrm{m}}} \approx \frac{\tilde{s}_\xi(\xi, \vec{G}; B_{\mathrm{m}})}{B_{\mathrm{m}}} \tag{34}$$

and the derivative of the Radon transform of can be estimated as

$$\frac{\partial p(\xi, \hat{\alpha}_G)}{\partial \xi} \approx \frac{1}{\cos^2 \alpha} \frac{\tilde{s}_\xi(\xi, \vec{G}; B_{\mathrm{m}})}{B_{\mathrm{m}}}. \tag{35}$$

Using this relationship, one can estimate $p(\xi, \hat{\alpha}_G)$ from its derivative, and reconstruct the density function $f_{\vec{r}}(\vec{r})$ according to Eq. (17) by use of a wide variety of reconstruction algorithms.

One can also reconstruct the derivative of $f_{\vec{r}}(\vec{r})$ directly from the estimate of the derivative of the Radon transform. Specifically, it can be shown that

$$\frac{\delta f_{\vec{r}}(B, c\vec{x})}{\delta B} = \mathcal{R}^{-1} \left[\cos \alpha \frac{\delta p(\xi, \hat{\alpha}_G)}{\delta \xi} \right] \approx \mathcal{R}^{-1} \left[\frac{\tilde{s}_\xi(\xi, \vec{G}; B_{\mathrm{m}})}{B_{\mathrm{m}} \cos \alpha} \right]. \tag{36}$$

The accuracy of the above particular set of methods relies on the assumption that the modulation amplitude is significantly less than the overall width of the narrowest resonance in the object. Under the small amplitude assumption, the width of the observed spectra will increase linearly with the modulation amplitude.

2.7. Reconstruction directly using the modulation distorted spectra

A second method for reconstructing the spectral–spatial image involves direct reconstruction from the acquired data, $\tilde{s}_\xi(\xi, \vec{G}; B_{\mathrm{m}})$, without any assumption that the modulation amplitude is small. The use of large modulation amplitudes will lead to distortion of the spectral shape, roughly described by broadening, and non-linear changes in the spectral amplitude. This, however, is distinct from being in the non-linear response limit where the physics of the absorption cannot be described by a linear Bloch equation. Modulation amplitudes on the order of the width of the spectral features can be used to increase the spectral amplitude and the SNR of the measured data. The dependence of spectral amplitude on modulation amplitude is well known for the basic spectral shapes [34], but is not well defined for spectra acquired with gradients and generally unknown spatial distributions. When overmodulation is used, we demonstrate that only the spectral, and not the spatial, distributions in the reconstructed images will include distortions due to the modulation. Extraction of the intrinsic spectral parameters requires appropriate spectral fitting to get an estimate of $f_{\vec{r}}(\vec{r})$ [38].

Analogous to the definitions of Eq. (21) and Eq. (22) for spectra collected with an applied field gradient, we may define the first harmonic signal detected from a point sample located at $\vec{x}$ with no magnetic field gradient as

$$\tilde{f}_{\vec{r}}(\vec{r}; B_{\mathrm{m}}) \equiv \frac{1}{T} \int_{-T}^{T} f_{\vec{r}}(B + B_{\mathrm{mod}}(t), c\vec{x}) \sin \omega_{\mathrm{m}} t \, \mathrm{d}t. \tag{37}$$

Thus, Eq. (29) can be re-expressed as

$$\mathcal{R}^{-1} \left[\frac{\tilde{s}_\xi(\xi, \vec{G}; B_{\mathrm{m}})}{\cos \alpha} \right] = \tilde{f}_{\vec{r}}(\vec{r}; B_{\mathrm{m}}). \tag{38}$$

Direct reconstruction from the modulation distorted spectra produces an image where the spectra associated with each spatial voxel are independently distorted according to the modulation conditions. As noted previously, the spatial distribution is unaffected by Zeeman

modulation. From this data, spectral fitting may be applied to provide an accurate estimate of undistorted spectral parameters at each point in the reconstructed image. A spectral fitting algorithm, such as that described by Robinson et al. [37], can be used to recover an estimate of $f_{\vec{r}}(\vec{r})$ from that of $\tilde{f}_{\vec{r}}(\vec{r}; B_m)$ made according to Eq. (38).

2.8. Integration of the modulated spectra prior to reconstruction

Direct reconstruction from the first harmonic projections results in a spectral–spatial image containing first harmonic spectra, as observed in Eq. (38). These first harmonic projections are not positive definite. However, non-negativity is not a necessary condition for many image reconstruction algorithms, including filtered back-projection and direct Fourier reconstruction. Other forms of image reconstruction, including many iterative techniques, do rely on positive definite projection data. One method to achieve a positive definite signal, for a pure absorption signal, is to integrate the measured spectra. This results in modulation-distorted absorption projections which can be used to reconstruct a spectral–spatial image. This integration modifies [38] to

$$\mathcal{R}^{-1}\left[\frac{\int \tilde{s}_\xi(\xi, \vec{G}; B_m)\, d\xi}{\cos^2\alpha}\right] = \int \tilde{f}_{\vec{r}}(B, c\vec{x}; B_m)\, dB. \qquad (39)$$

Note that the integrals in [39] are indefinite. The reconstructed spectral–spatial image contains modulation distorted absorption spectra. As discussed above, spectral fitting can be used to estimate the undistorted spectral parameters. This method of image reconstruction was used for the conventional and overmodulated images presented by Mailer et al. [38], which demonstrate the fact that spectral shape is affected by modulation amplitude while the spatial resolution is not affected.

3. Discussion

In this work, we have described an explicit model of EPR imaging, including the effects of modulation amplitude, and the relationship between the measured EPR data and the Radon transform of the spectral–spatial object. Several methods of image reconstruction suggested by this theoretical development were discussed. We have also shown that the effect of modulation amplitude on the reconstructed image is restricted to the spectral dimension and that the spatial distribution is unaffected. Thus, in spectroscopic EPR imaging, overmodulation does not lead to a decrease in spatial resolution. The ability to use high modulation amplitudes in EPR imaging significantly improves the observed SNR and the precision of estimated spectral parameters [38].

The mathematical expressions developed in this work are the starting point for a number of published enhancements in the literature for computed tomography. These include the adaptive filtering technique [43], iterative reconstruction techniques [44], techniques for use with truncated data [45] and few–view reconstruction [46]. The development of a consistent description of the backprojection problem will allow such enhancements to be applied in the specific context of EPR image reconstruction. In addition, this mathematical framework may enable further improvements in image quality and imaging flexibility through the incorporation of appropriate perturbation terms.

Acknowledgments

References

[1] G.R. Eaton, S.S. Eaton, K. Ohno, EPR Imaging and In Vivo EPR, CRC Press, Boca Raton, 1991, 321 pp.

[2] P. Kuppusamy, M. Chzhan, J. Zweier, Principles of imaging, in: L.J. Berliner (Ed.), In Vivo EPR (ESR) Theory and Applications. Vol. 18, Biological Magnetic Resonance, Kluwer Academic/Plenum Publishers, New York, 2004, pp. 99–152.

[3] H.J. Halpern, C. Yu, M. Peric, E.D. Barth, G.S. Karczmar, J.N. River, D.J. Grdina, B.A. Teicher, Measurement of differences in pO_2 in response to perfluorocarbon/carbogen in FSa and NFSa murine fibrosarcomas with low-frequency electron paramagnetic resonance oximetry, Radiat. Res. 145 (5) (1996) 610–618.

[4] H.J. Halpern, C. Yu, M. Peric, E. Barth, D.J. Grdina, B.A. Teicher, Oxymetry deep in tissues with low-frequency electron paramagnetic resonance, Proc. Natl. Acad. Sci. USA 91 (26) (1994) 13047–13051.

[5] S. Subramanian, K. Yamada, A. Irie, R. Murugesan, J.A. Cook, N. Devasahayam, G.M. Van_Dam, J.B. Mitchell, M.C. Krishna, Noninvasive in vivo oximetric imaging by radiofrequency FT EPR, Magn. Reson. Med. 47 (5) (2002) 1001–1008.

[6] M. Velayutham, H. Li, P. Kuppusamy, J.L. Zweier, Mapping ischemic risk region and necrosis in the isolated heart using EPR imaging, Magn. Reson. Med. 49 (6) (2003) 1181–1187.

[7] G. He, A. Samouilov, P. Kuppusamy, J.L. Zweier, In vivo imaging of free radicals: applications from mouse to man, Mol. Cell. Biochem. 234–235 (1–2) (2002) 359–367.

[8] H.J. Halpern, Stable Soluble Paramagnetic Compounds. Vol. 18, Biological Magnetic Resonance, in: L.J. Berliner (Ed.), In Vivo EPR (ESR) Theory and Applications, Kluwer Academic/Plenum Publishers, New York, 2004, pp. 201–232.

[9] H.J. Halpern, C. Yu, E. Barth, M. Peric, G.M. Rosen, In situ detection, by spin trapping, of hydroxyl radical markers produced from ionizing radiation in the tumor of a living mouse, Proc. Natl. Acad. Sci. USA 92 (3) (1995) 796–800.

[10] M. Elas, B.B. Williams, A. Parasca, C. Mailer, C.A. Pelizzari, M.A. Lewis, J.N. Rivers, G.S. Karczmar, E.D. Barth, H.J.

Halpern, Quantitative tumor oxymetric images from 4D electron paramagnetic resonance imaging (EPRI): methodology and comparison with blood oxygen level-dependent (BOLD) MRI, Magn. Reson. Med. 49 (4) (2003) 682–691.

[11] H.J. Halpern, M. Peric, C. Yu, E.D. Barth, G.V.R. Chandramouli, M.W. Makinen, G.M. Rosen, In vivo spin-label murine pharmacodynamics using low-frequency electron paramagnetic resonance imaging, Biophys. J. 71 (1) (1996) 403–409.

[12] P. Kuppusamy, H. Li, G. Ilangovan, A.J. Cardounel, J.L. Zweier, K. Yamada, M.C. Krishna, J.B. Mitchell, Noninvasive imaging of tumor redox status and its modification by tissue glutathione levels, Cancer Res. 62 (1) (2002) 307–312.

[13] V.V. Khramtsov, I.A. Grigor'ev, M.A. Foster, D.J. Lurie, I. Nicholson, Biological applications of spin pH probes, Cell. Mol. Biol. (Noisy-le-grand) 46 (8) (2000) 1361–1374.

[14] H.J. Halpern, G.V. Chandramouli, E.D. Barth, C. Yu, M. Peric, D.J. Grdina, B.A. Teicher, Diminished aqueous microviscosity of tumors in murine models measured with in vivo radiofrequency electron paramagnetic resonance, Cancer Res. 59 (22) (1999) 5836–5841.

[15] S.S. Velan, R.G. Spencer, J.L. Zweier, P. Kuppusamy, Electron paramagnetic resonance oxygen mapping (EPROM): direct visualization of oxygen concentration in tissue, Magn. Reson. Med. 43 (6) (2000) 804–809.

[16] J.H. Ardenkjaer-Larsen, I. Laursen, I. Leunbach, G. Ehnholm, L.G. Wistrand, J.S. Petersson, K. Golman, EPR and DNP properties of certain novel single electron contrast agents intended for oximetric imaging, J. Magn. Reson. 133 (1) (1998) 1–12.

[17] T. Reddy, T. Iwama, H. Halpern, V. Rawal, General synthesis of persistent trityl radicals for EPR imaging of biological systems, J. Org. Chem. 67 (14) (2002) 4635–4639.

[18] H.J. Halpern, D.P. Spencer, J. van Polen, M.K. Bowman, R.J. Massoth, A.C. Nelson, E.M. Dowey, B.A. Teicher, An imaging radiofrequency electron spin resonance spectrometer with high resolution and sensitivity for in vivo measurements, Rev. Sci. Instrum. 60 (1989) 1040–1050.

[19] M. Alecci, S.D. Penna, A. Sotgiu, L. Testa, I. Vannucci, Electron paramagnetic resonance spectrometer for three-dimensional in vivo imaging at very low frequency, Rev. Sci. Instrum. 63 (1992) 4263.

[20] R.W. Quine, G.A. Rinard, S.S. Eaton, G.R. Eaton, A pulsed and continuous wave 250 MHz electron paramagnetic resonance spectrometer, Concepts Magn. Reson. 15 (1) (2002) 59–61.

[21] R. Murugesan, M. Afeworki, J.A. Cook, Devasahayam Nallathamby, R. Tschudin, J.B. Mitchell, S. Subramanian, M.C. Krishna, A broadband pulsed radio frequency electron paramagnetic resonance spectrometer for biological applications, Rev. Sci. Instrum. 69 (4) (1998) 1869–1876.

[22] J. Koscielniak, N. Devasahayam, M.S. Moni, P. Kuppusamy, K. Yamada, J.B. Mitchell, M.C. Krishna, S. Subramanian, 300 MHz continuous wave electron paramagnetic resonance spectrometer for small animal in vivo imaging, Rev. Sci. Instrum. 71 (11) (2000) 4273–4281.

[23] P.-M.L. Robitaille, R. Warner, J. Jagadeesh, A.M. Abduljalil, A. Kangarlu, R.E. Burgess, Y. Yu, L. Yang, H. Zhu, Z. Jiang, et al., Design and assembly of an 8 T whole-body MR scanner, J. Comput. Assisted Tomogr. 23 (6) (1999) 808–820.

[24] W. Froncisz, J.S. Hyde, The loop-gap resonator: a new microwave lumped circuit ESR sample structure, J. Magn. Reson. 47 (3) (1982) 515–521.

[25] N. Devasahayam, S. Subramanian, R. Murugesan, J.A. Cook, M. Afeworki, R.G. Tschudin, J.B. Mitchell, M.C. Krishna, Parallel coil resonators for time-domain radiofrequency electron paramagnetic resonance imaging of biological objects, J. Magn. Reson. 142 (1) (2000) 168–176.

[26] G. He, S. Petryakov, A. Samouilov, M. Chzhan, P. Kuppusamy, J.L. Zweier, Development of a resonator with automatic tuning and coupling capability to minimize sample motion noise for in vivo EPR spectroscopy, J. Magn. Reson. 149 (2) (2001) 218–227.

[27] P.C. Lauterbur, D.N. Levin, R.B. Marr, Theory and simulation of NMR spectroscopic imaging and field plotting by projection reconstruction involving an intrinsic frequency dimension, J. Magn. Reson. 59 (3) (1984) 536–541.

[28] M.M. Maltempo, Differentiation of spectral and spatial components in EPR imaging using 2-D image reconstruction algorithms, J. Magn. Reson. 69 (1) (1986) 156–161.

[29] M.M. Maltempo, S.S. Eaton, G.R. Eaton, Spectral–spatial two-dimensional EPR imaging, J. Magn. Reson. 72 (3) (1987) 449–455.

[30] R.K. Woods, W.B. Hyslop, R.B. Marr, P.C. Lauterbur, Image reconstruction, in: G.R. Eaton, S.S. Eaton, K. Ohno (Eds.), EPR Imaging and In Vivo EPR, CRC Press, Boca Raton, 1991, pp. 91–118.

[31] S.S. Eaton, M.M. Maltempo, E.D.A. Stemp, G.R. Eaton, Three-dimensional EPR imaging with one spectral and two spatial dimensions, Chem. Phys. Lett. 142 (1987) 567–569.

[32] P. Kuppusamy, M. Chzhan, A. Samouilov, P. Wang, J.L. Zweier, Mapping the spin-density and lineshape distribution of free radicals using 4D spectral–spatial EPR imaging, J. Magn. Reson. Series B 107 (2) (1995) 116–125.

[33] X. Pan, B.B. Williams, H.J. Halpern, 3D and 4D EPRI: a theoretical investigation, in: VII Internationl Conference on Fully 3D Reconstruction in Radiology and Nuclear Medicine, Saint-Malo, France, 2003.

[34] C.P. Poole, Electron Spin Resonance: A Comprehensive Treatise on Experimental Techniques, Wiley, New York, 1967.

[35] M. Peric, H.J. Halpern, Fitting of the derivative Voigt ESR line under conditions of modulation broadening, J. Magn. Reson. A 109 (1994) 198–202.

[36] J. Hyde, M. Pasenkiewicz-Gierula, A. Jesmanowicz, W. Antholine, Pseudo field modulation in EPR spectroscopy, Appl. Magn. Reson. 1 (1990) 483–496.

[37] B.H. Robinson, C. Mailer, A.W. Reese, Linewidth analysis of spin labels in liquids. I. Theory and data analysis, J. Magn. Reson. 138 (2) (1999) 199–209.

[38] C. Mailer, B.H. Robinson, B.B. Williams, H.J. Halpern, Spectral fitting: the extraction of crucial information from a spectrum and a spectral image, Magn. Reson. Med. 49 (2003) 1175–1180.

[39] E.T. Quinto, The invertibility of rotation invariant radon transforms, J. Math. Anal. Appl. 91 (2) (1983) 510–522.

[40] A.M. Cormack, The radon-transform on a family of curves in the plane, Proc. Am. Math. Soc. 83 (2) (1981) 325–330.

[41] G. Beylkin, The inversion problem and applications of the generalized Radon-transform, Commun. Pure Appl. Math. 37 (5) (1984) 579–599.

[42] H. Wahlquist, Modulation broadening of unsaturated Lorentzian lines, J. Chem. Phys. 35 (5) (1961) 1708–1710.

[43] C.-M. Kao, X. Pan, Non-iterative methods incorporating a priori source distribution and data information for suppression of image noise and artefacts in 3D SPECT, Phys. Med. Biol. 45 (2000) 2801–2819.

[44] J.A. Fessler, Statistical image reconstruction methods for transmission tomography, in: M. Sonka, J.M. Fitzpatrick (Eds.), Handbook of Medical Imaging, Vol. 2, SPIE Press, Bellingham, Washington, USA, 2000, pp. 1–70.

[45] A. Ramm, A.I. Zaslavsky, The Radon Transform and Local Tomography, CRC Press, Boca Raton, FL, 1993.

[46] P.J. La Riviere, X. Pan, Noise properties of periodic interpolation methods with implications for few view tomography, IEEE Trans. Nucl. Sci. 46 (1999) 639–645.